arXiv:astro-ph/0503029v1 2 Mar 2005

Revision according to the second referee's comments

Discovery of Extremely Embedded X-ray Sources in the R Coronae Australis Star Forming Core

Kenji Hamaguchi[1], Michael F. Corcoran[2], Rob Petre, Nicholas E. White

Exploration of the Universe Division, Goddard Space Flight Center, Greenbelt, MD 20771, USA

kenji@milkyway.gsfc.nasa.gov; corcoran@lheapop.gsfc.nasa.gov; robert.Petre-1@nasa.gov; nwhite@lheapop.gsfc.nasa.gov

and

Beate Stelzer

INAF, Osservatorio Astronomico di Palermo, Piazza del Parlamento 1, I-90134 Palermo, Italy

stelzer@astropa.unipa.it

and

Ko Nedachi, Naoto Kobayashi

Institute of Astronomy, University of Tokyo, 2-21-1 Osawa, Mitaka, Tokyo 181-0015, Japan

nedachi@subaru.naoj.org; naoto@ioa.s.u-tokyo.ac.jp

and

Alan T. Tokunaga

Institute for Astronomy, University of Hawaii, 2680 Woodlawn Drive, Honolulu, HI 96822, USA

tokunaga@ifa.hawaii.edu

[1]National Research Council, 500 Fifth Street, NW, Washington, D.C. 20001, USA

[2]Universities Space Research Association, 7501 Forbes Blvd, Ste 206, Seabrook, MD 20706, USA

ABSTRACT

With the *XMM-Newton* and *Chandra* observatories, we detected two extremely embedded X-ray sources in the R Corona Australis (R CrA) star forming core, near IRS 7. These sources, designated as X_E and X_W, have X-ray absorption columns of $\sim 3 \times 10^{23}$ cm^{-2} equivalent to $A_V \sim 180^m$. They are associated with the VLA centimeter radio sources 10E and 10W, respectively. X_W is the counterpart of the near-infrared source IRS 7, whereas X_E has no K-band counterpart above 19.4^m. This indicates that X_E is younger than typical Class I protostars, probably a Class 0 protostar or in an intermediate phase between Class 0 and Class I. The X-ray luminosity of X_E varied between $29 < \log L_X < 31.2$ ergs s^{-1} on timescales of 3–30 months. X_E also showed a monotonic increase in X-ray brightness by a factor of two in 30 ksec during an *XMM-Newton* observation. The *XMM-Newton* spectra indicate emission from a hot plasma with $kT \sim 3$–4 keV and also show fluorescent emission from cold iron. Though the X-ray spectrum from X_E is similar to flare spectra from Class I protostars in luminosity and temperature, the light curve does not resemble the lightcurves of magnetically generated X-ray flares because the variability timescale of X_E is too long and because variations in X-ray count rate were not accompanied by variations in spectral hardness. The short-term variation of X_E may be caused by the partial blocking of the X-ray plasma, while the month-long flux enhancement may be driven by mass accretion.

Subject headings: stars: activity — stars: magnetic fields — stars: pre–main-sequence — stars: rotation — X-rays: stars

1. Introduction

Low-mass protostars are divided into two classes, Class 0 and Class I, according to their infrared (IR) and radio spectral energy distribution (SED). This classification generally traces their evolutionary status. Class 0 objects are thought to be young ($t \sim 10^4$ yr) protostars which mainly emit in the far-IR and submillimeter wavelengths with blackbody temperatures of <30 K (André et al. 1993). They are believed to be accreting mass dynamically from their huge circumstellar envelopes. Class I objects are believed to be older protostars ($t \sim 10^5$ yr) at the end of the mass-accretion phase and emit in the near-IR at temperatures of $T \sim 3000-5000$ K.

Protostellar cores are generally hidden inside enormous gas envelopes. Hard X-rays can penetrate the thick molecular clouds, and hard X-ray observations have revealed high energy activity associated with Class I objects (Koyama et al. 1996; Grosso et al. 1997; Imanishi et al. 2001). The observed X-ray emission exhibits occasional rapid outbursts reminiscent of solar flares though current star formation theories do not predict solar-type magnetic dynamos in very young stars. Montmerle et al. (2000) proposed an alternative dynamo mechanism, in which fossil magnetic fields link the protostellar core with its circumstellar disk reconnect.

Hard X-ray emission from other embedded sources was reported in the OMC-2/3 cloud (Tsuboi et al. 2001). The two detected sources show Class 0 characteristics: huge absorption ($N_{\rm H} \sim 1 - 3 \times 10^{23}{\rm cm}^{-2}$), no near-IR counterparts, and associations with millimeter radio clumps. However, follow-up radio and near-IR observations by Tsujimoto et al. (2004) did not unambiguously classify them as Class 0 protostars. In particular, one of these sources correlates with a centimeter radio source and a jet feature in the H_2 band, which indicates excitation by a jet from a nearby Class I protostar. Though Skinner et al. (2003) and Rho et al. (2004) have reported X-ray emission from other millimeter radio clumps in NGC 2024 and the Trifid nebula, the photon statistics in those observations were too limited ($\lesssim$50 photons per source) to identify their nature conclusively. To date no X-ray source has been clearly identified with a bona-fide Class 0 object.

The R Corona Australis (R CrA) cloud is a nearby star forming region (d ∼170 pc, Knude & Hϕg 1998). Among many young stellar objects in the cloud, those in the IRS 7 region have attracted particular interest as a site of ongoing star formation. The region contains double peaked, strong centimeter emission; an eastern peak is designated as 10E or IRS 7B, and a western peak is designated 10W or IRS 7A (Brown 1987; Feigelson et al. 1998; Harju et al. 2001). It also contains two submillimeter peaks (van den Ancker 1999), multiple millimeter continuum peaks (Henning et al. 1994; Saraceno et al. 1996; Chini et al. 2003; Choi & Tatematsu 2004), and a signature of strong bipolar outflows (Harju et al. 1993; Anderson et al. 1997), but only one near-IR source, IRS 7 (Wilking et al. 1997, W97). These characteristics make the IRS 7 region a promising host of Class 0 sources. Koyama et al. (1996) detected hard X-ray emission and an intense flare from the IRS 7 region, which suggested the presence of a magnetically active protostar.

In this paper, we report the X-ray detection of two extremely embedded sources in the IRS 7 star forming core during *XMM-Newton* observations in 2003. These results, combined with the analysis of two *Chandra* observations carried out in 2000 and 2003, and follow-up near-IR observations with the University of Hawaii 88-inch Telescope (UH88), help to determine the nature of the detected X-ray sources.

2. X-ray Observations and Absolute Position Correction

We analyzed X-ray data obtained with the *XMM-Newton* observatory on 2003 March 28 and 2003 March 29 (hereafter $\mathrm{Obs_{XMM1}}$ and $\mathrm{Obs_{XMM2}}$, see Table 1 for details). The *XMM-Newton* satellite (Jansen et al. 2001) is composed of three nested Wolter I type X-ray telescopes (Aschenbach et al. 2000) with European Photon Imaging Camera (EPIC) CCD detectors in their focal planes (Strüder et al. 2001; Turner et al. 2001). The observations were obtained with the EPIC pn and EPIC MOS1 and EPIC MOS2 detectors, in full frame mode with the medium filter. We pointed at similar sky positions in $\mathrm{Obs_{XMM1}}$ and $\mathrm{Obs_{XMM2}}$; the IRS 7 star forming core was at $6'$ off-axis, where the 90% photon radius is $\sim 1'$. We analyzed the X-ray data using the software package SAS ver. 5.4.1 and HEAsoft ver. 5.2. We first processed the data using the SAS scripts "emchain" and "epchain", and screened out high background periods using standard criteria, excluding events when the entire chip count rate of "pattern = 0" events above 10 keV was >0.35 cnts $\mathrm{s^{-1}}$ for MOS and >1 cnts $\mathrm{s^{-1}}$ for pn, and excluding events close to hot pixels or outside the field of view. Finally, we selected events with pattern $\leqq 4$ for spectral analysis of the EPIC pn and with pattern $\leqq 12$ for the EPIC MOS and the other analyses of the EPIC pn.

To help source identification and investigate long-term flux variations, we analyzed two archival *Chandra* observations. *Chandra* has a single high-performance X-ray telescope which provides sub-arcsecond imaging (Weisskopf et al. 2002). The *Chandra* observations were obtained using the Advanced CCD Imaging Spectrometer detector using the Imaging array (ACIS-I) on 2000 October 7 and 2003 June 26 (hereafter $\mathrm{Obs_{CXO1}}$ and $\mathrm{Obs_{CXO2}}$, see Table 1). Garmire & Garmire (2002) presented the first results of $\mathrm{Obs_{CXO1}}$. The IRS 7 star forming region was at $2'$ and $0.'2$ off-axis in $\mathrm{Obs_{CXO1}}$ and $\mathrm{Obs_{CXO2}}$, respectively, where the 90% photon radius is $\sim 1''$. We analyzed the *Chandra* data using the software packages CIAO ver. 2.3 and HEAsoft ver. 5.2. For $\mathrm{Obs_{CXO1}}$, we reprocessed the level 1 event data with "acis_process_events" to compensate for degradation of the CCD spectral resolution by charge transfer inefficiency (CTI, Townsley et al. 2000). For $\mathrm{Obs_{CXO2}}$, we used pipeline-processed level 2 event data which was already corrected for CTI degradation. Finally, we selected events from both observations with the standard grades 0, 2, 3, 4, and 6 in the *ASCA* event grade system for further analysis.

For the correction of the absolute coordinates, we measured positions of X-ray bright sources on the combined EPIC pn plus MOS images between 0.3−10 keV and positions of sources in the ACIS-I image between 0.5−9 keV using available source detection packages (SAS: *edetect_chain*, CIAO: *wavdetect*, see also Table 1). We correlated these positions with near-IR source positions in the 2MASS All-Sky Point Source Catalog (PSC) obtained from

the NASA/IPAC Infrared Science Archive (GATOR)[1], whose astrometric accuracy is good to about 0.″ 1[2]. Each X-ray source has only one 2MASS counterpart within 4″, so that the source identification is very reliable. After adjusting the X-ray positions to the 2MASS positions, the deviation of the *Chandra* and *XMM-Newton* coordinates from the 2MASS coordinates is $\lesssim$ 0.″ 6.

3. X-ray Image

Figure 1 shows a "true-color" X-ray image of the R CrA star forming region, which combines EPIC pn and MOS(1+2) data taken in both $\mathrm{Obs_{XMM1}}$ and $\mathrm{Obs_{XMM2}}$. Red, green, and blue colors in the image represent soft (0.2−1 keV), medium (1−3 keV), and hard (3−9 keV) bands, respectively. The IRS 7 region is colored in dark blue, which indicates the presence of hard X-ray sources, possibly suffering strong low-energy absorption. The top left panel of Figure 2 shows a detailed view of the IRS 7 region of the hard band image. A strong X-ray source, labelled $\mathrm{X_E}$, was detected with *edetect_chain* in both $\mathrm{Obs_{XMM1}}$ and $\mathrm{Obs_{XMM2}}$ (Table 2). Though *edetect_chain* failed to detect a small peak on the tail of the *psf* to the north-west of $\mathrm{X_E}$, our subsequent analysis using the $\mathrm{Obs_{XMM1}}$ data confirmed it as a weak source at $\sim 14\sigma$ significance which we labelled $\mathrm{X_W}$. The positional accuracy of both sources is hard to estimate because the sources are unresolved. In this paper, we tentatively put the errors at $\sim$2″, the half pixel size of the EPIC pn camera. If we rely on the result of *edetect_chain*, the absolute position accuracy of $\mathrm{X_E}$ is 1.″ 7 for $\mathrm{Obs_{XMM1}}$ and 1.″ 2 for $\mathrm{Obs_{XMM2}}$ at 90% confidence.

Chandra detected two weak X-ray sources in the IRS 7 region at above 4σ significance in both $\mathrm{Obs_{CXO1}}$ and $\mathrm{Obs_{CXO2}}$ (top right panel of Figure 2 for $\mathrm{Obs_{CXO1}}$, Table 2). Though each source has less than 20 photons, the absolute source positions are determined within 1″ thanks to the excellent spatial resolution of *Chandra*. These detected sources have corresponding *XMM-Newton* sources though, if we take the error circles derived using the *edetect_chain* results, the source positions of $\mathrm{X_E}$ between the *Chandra* and *XMM-Newton* observations have a significant discrepancy of $\sim$2″. Hereafter, we refer to the *Chandra* detected positions for both sources.

The bottom panels of Figure 2 compare the X-ray source positions with sources detected at other wavelengths. $\mathrm{X_E}$ is associated with the VLA centimeter source 10E (Brown 1987)

[1]http://irsa.ipac.caltech.edu/applications/Gator/

[2]Sect. 2.2 of Explanatory Supplement to the 2MASS All-Sky Data Release: http://www.ipac.caltech.edu/2mass/releases/allsky/doc/

and the sub-millimeter peak vdA 5 (van den Ancker 1999). Choi & Tatematsu (2004) also suggested a marginal millimeter source at the position of X_E. X_W is associated with centimeter (10W in Brown 1987), millimeter (source 4 in Choi & Tatematsu 2004), and sub-millimeter sources, and the near-IR source, IRS 7 (see also section 5).

4. X-ray Light Curves and Spectra

4.1. East Source (X_E)

We extracted source photons from the *XMM-Newton* observations of X_E from a 27.″ 5 radius circle centered on the source position excluding the region around X_W, with background taken from appropriate source free regions. We obtained ∼2,000 net counts from Obs_{XMM1} and Obs_{XMM2}, enabling us to perform detailed timing and spectral analyses. For the *Chandra* data, we extracted events from a 1.″ 8 radius circle centered on the source position. The background level was negligibly low. Only 10−20 counts were extracted from the *Chandra* observation, which precludes detailed spectral analysis.

The top panel of Figure 3 shows the background subtracted EPIC pn+MOS light curve of X_E in the 2−10 keV band. The first half of the light curve, corresponding to Obs_{XMM1}, is mostly flat with some indications of a slight increase at the end. A constant provides an acceptable χ^2 fit at above 90% confidence (Table 3). The source was about four times brighter than the average count rate of Obs_{XMM1} at the beginning of the second half, corresponding to Obs_{XMM2}, and the count rate gradually increased by a factor of two. This part of the light curve can be acceptably fit at greater than 90% confidence level by a linear increase with a slope of $\sim 9.3 \times 10^{-2}$ cnts s^{-1} day^{-1}(Table 3). During both observations, the hardness ratio defined as count rates in the 5−10 keV band over those in the 2−5 keV band remained unchanged, except for a minimum at 7.86 days. This means that time variation in count rate was not accompanied by any significant change of the spectral shape. On the other hand, the light curves show marginal dips on timescales of <1 ksec near 8.02 and 8.17 days. These dips are seen in both the pn and MOS light curves of X_E and other nearby sources, such as R CrA, IRS 5, and CrA 1, have no dips at those times. These facts do not support an instrumental origin. We note that these dips might suggest a tentative period of ∼13.9 ksec, with the combination of minimal dips at 6.56 and 7.85 days (the dip at 7.85 day was only covered with the MOS data and does not appear in the Figure 3).

The EPIC spectra of X_E in Obs_{XMM1} and Obs_{XMM2} (Figure 4) show several similarities: significant emission up to ∼10 keV; strong absorption below 2−3 keV; a broad line feature between 6−7 keV; marginal lines between 5−6 keV in the EPIC pn spectra (which may

be of instrumental or cosmic origin[3]). To investigate the 6−7 keV line feature, we fit the EPIC pn and MOS (1+2) spectra simultaneously with an absorbed power-law model with a Gaussian component. An acceptable fit above 90% confidence has a photon index of 3.0 (2.5–3.4), a Gaussian line centroid of 6.60 (6.53–6.67) keV, and a Gaussian width of 0.15 (0.079–0.28) keV, where the numbers in parentheses denote the 90% confidence range. The derived Gaussian width, equivalent to Δv ∼7,000 km s^{-1} if produced by Doppler broadening, is unreasonably large for a stellar plasma (see also discussion 6.1). We therefore interpret the broad feature as a blend of iron lines from a hot plasma at 6.7 keV and a fluorescent iron line at 6.4 keV though the profile needs to be confirmed with deeper observations. We then fit the *XMM-Newton* spectra with XSPEC by an absorbed 1-temperature (1T) optically thin, thermal plasma model (wabs: Morrison & McCammon 1983; MeKaL: Mewe et al. 1995) with a Gaussian component with line center fixed at 6.4 keV. For either of the two observations this model yields acceptable fits at the 90 % confidence level (Model A and B in Table 4). $N_{\rm H}$ differs significantly between Obs$_{\rm XMM1}$ and Obs$_{\rm XMM2}$, possibly due to the simplistic spectral model we assumed. Indeed, the soft emission below 3 keV was unchanged between Obs$_{\rm XMM1}$ and Obs$_{\rm XMM2}$, suggesting an additional component along with the hard emission. In the single temperature fit to Obs$_{\rm XMM1}$, the soft emission is included as a part of the absorption slope whereas the fit to Obs$_{\rm XMM2}$ determines $N_{\rm H}$ from the 3−5 keV slope and does not reflect the soft emission. We therefore refit the spectra of Obs$_{\rm XMM1}$ and Obs$_{\rm XMM2}$ simultaneously with an absorbed 2T model — 1T for the variable hard component and 1T for the constant soft component — with a Gaussian line at 6.4 keV. In this model, we tied the $N_{\rm H}$ of the hard components in Obs$_{\rm XMM1}$ and Obs$_{\rm XMM2}$ and tied the elemental abundances of all components. We allowed $N_{\rm H}$ of the soft and hard components to be fit independently because a model fit with a common $N_{\rm H}$ gives large $N_{\rm H}$ ∼2.4×10^{23} cm^{-2} and hence an unrealistically large intrinsic log $L_{\rm X}$ ∼ 35 ergs s^{-1} for the soft component. The model, again, successfully reproduced the spectra above the 90% confidence level (Model C in Table 4). The derived physical parameters of the hard component are at the higher end among those of Class I protostars (e.g., see Imanishi et al. 2001, for comparison): large $N_{\rm H}$ ∼2.8×10^{23} cm^{-2}, equivalent to $A_{\rm V}$ ∼180^m (using the $N_{\rm H}$ − $A_{\rm V}$ relation by Imanishi et al. (2001)); plasma temperature of 3–4 keV; log $L_{\rm X}$ ∼30.8 ergs s^{-1} in Obs$_{\rm XMM1}$, which further increased to ∼31.2 ergs s^{-1} in Obs$_{\rm XMM2}$; and a fluorescent iron line equivalent width (EW) of ∼810 (240−1400) eV in Obs$_{\rm XMM1}$ and ∼250 (100−400) eV in Obs$_{\rm XMM2}$. Meanwhile, the metal abundance is ∼0.2 (0.1−0.3) solar, which is typical of low-mass young stars (e.g. Favata et al. 2003).

[3]Sect. 3.3.7.2 in *XMM-Newton* Users Handbook,
http://xmm.vilspa.esa.es/external/xmm_user_support/documentation/uhb/index..html

Since we have very few counts from the *Chandra* observations, we simply calculated a softness ratio, defined as S / (H + S), where S and H are photon counts in the 0.5–3 keV and 3–9 keV bands, respectively. The ratios are 0.15±0.08 (S = 3, H = 17) in $\mathrm{Obs_{CXO1}}$ and 0.38±0.13 (S = 5, H = 8) in $\mathrm{Obs_{CXO2}}$ where the errors show 1-sigma. The same softness ratios evaluated for the *XMM-Newton* best-fit models after adjusting to the *Chandra* ACIS-I response are 0.11 for $\mathrm{Obs_{XMM1}}$ and 0.048 for $\mathrm{Obs_{XMM2}}$, suggesting that the spectra have been softer during the *Chandra* observations. This is consistent with the picture that the hard component further declined during the *Chandra* observations while the soft component was unchanged.

4.2. West Source ($\mathrm{X_W}$)

We extracted *XMM-Newton* source events of $\mathrm{X_W}$ from an ellipse with axes 15″ by 10.″5 elongated toward the NNE direction, excluding a region with strong contamination from $\mathrm{X_E}$, and selected the background from a symmetrical region near $\mathrm{X_E}$. We did not use the $\mathrm{Obs_{XMM2}}$ data, because the $\mathrm{X_W}$ region suffered strong contamination from $\mathrm{X_E}$. For the *Chandra* data, we extracted source events from a 1.″8 radius circle. The background level was negligibly low.

The *XMM-Newton* spectra were reproduced by an absorbed 1T model with $N_{\mathrm{H}} \sim 3.4\times10^{23}$ $\mathrm{cm^{-2}}$, $kT > 1.6$ keV, and $\log L_{\mathrm{X}} \sim 30.5$ ergs $\mathrm{s^{-1}}$ (left panel of Figure 5, Model D in Table 4). We added both spectra from $\mathrm{Obs_{CXO1}}$ and $\mathrm{Obs_{CXO2}}$ because their count rates are about the same. The summed spectrum can be reproduced by the best-fit *XMM-Newton* model just by changing its normalization (right panel of Figure 5, Model E in Table 4).

5. Follow-up Observations in the Near-IR

Infrared source catalogues in the R CrA region currently available have several shortcomings: shallow limiting magnitude (e.g. $K_{limit} \sim 15^m$ for 2MASS, 16.5^m for W97); insufficient spatial resolution (e.g. 1″ $\mathrm{pix^{-1}}$ for 2MASS and 0.″75 $\mathrm{pix^{-1}}$ for W97); and insufficient positional accuracy (e.g., ±1″ for W97). We therefore analyzed two deep K-band images of the field obtained in August 1998 and August 2003 using UH88 and the near-IR imager QUIRC. During the observations, we used the f/10 secondary mirror, yielding a pixel scale of 0.″1886 $\mathrm{pix^{-1}}$. The spatial resolution of our images is 0.″5 and 0.″8 in FWHM for the 1998 and 2003 data respectively. Both images were aligned with an accuracy of 0.″3 by referring to the coordinates of R CrA in the 2MASS catalogue and a high resolution image (FWHM

$\sim$0.″ 14) obtained with the SUBARU telescope. The analysis was made with IRAF[4].

Both images show R CrA as a filamentary and mildly extended reflection nebulae (Figure 6 for the 1998 data), but the location of X_E shows no significant emission, though it does have some marginal enhancement. The flux upper-limit was measured by subtracting the extended nebular emission, which we estimated with a third-order polynomial surface fit. The 5-σ upper-limit of X_E within the 20 $\times$ 20 pixel box centered at X_E was $\sim 19.4^m$ for the 1998 image and $\sim 19^m$ for the 2003 image. Meanwhile, using the SUBARU image (Nedachi et al. in preparation), we measured the absolute position of IRS 7 at (α_{2000}, δ_{2000}) = ($19^h 1^m 55.^s 34$, -36° 57′ 21.″ 69) with an accuracy of 0.″ 3. This is much more accurate than the earlier observations. With this new position, IRS 7 falls within the positional error circle of X_W (see the bottom right panel of Figure 2).

6. Discussion

6.1. The Nature and X-ray Emission Mechanism of X_E

Harju et al. (2001) suggested that the radio counterpart of X_E, source 10E, might be a radio galaxy or Galactic microquasar. However, AGNs with the observed X-ray flux above 2$-$8 $\times 10^{-13}$ ergs cm^{-2} s^{-1} (2$-$10 keV) are found $\lesssim$10 degree $^{-2}$ in the sky (Ueda et al. 1998), and the probability to detect such an AGN in the IRS 7 star forming core ($\sim$10arcsec^2) is extremely small ($\lesssim 10^{-4}$). Furthermore, AGNs do not generally show thermal iron K emission line and have rather flat spectral slopes ($\Gamma \leq 2$) (Ueda et al. 1998). Similarly, Galactic black hole candidates also show flat power-law X-ray spectra with $\Gamma = 1.5 - 2.1$ though they sometimes show thermal spectra with $kT \sim$0.5–1.5 keV (McClintock & Remillard 2003). Taking its association to the star forming core into account, X_E is most likely a very young stellar object.

Compared to Class I objects in the R CrA star forming region such as IRS 1, 2, and 5 which have $N_H \sim 2\times 10^{22}$ cm^{-2} and $K \lesssim 11^m$ (from our additional analysis of the Obs_{XMM1} and Obs_{XMM2} data; see also W97), X_E shows much larger X-ray absorption and much smaller near-IR luminosity. X_E is also associated with the strong submillimeter condensation vdA 5 (van den Ancker 1999). All these suggest that X_E is much younger than typical Class I objects, and that it is a Class 0 object or an object in an intermediate phase between Class 0

[4]IRAF is distributed by the National Optical Astronomy Observatories, which are operated by the Association of Universities for Research in Astronomy, Inc., under cooperative agreement with the National Science Foundation.

and Class I. We note that extremely embedded sources in the OMC-2/3 cloud have similarly high absorption columns of $N_{\rm H} \sim (1-3) \times 10^{23}$ cm^{-2} (Tsuboi et al. 2001).

Between the *Chandra* and *XMM-Newton* observations, $X_{\rm E}$ exhibited strong long-term X-ray variation by a factor of 10−100 on a timescale of a month (Figure 7). In none of the observations did we detect obvious flare activity though $\rm Obs_{XMM2}$ showed a marked flux increase. Active stars such as RS CVn and young stars in open clusters do not generally vary in X-rays more than a factor of 2−3 outside flares (Stern 1998). Less active stars such as the Sun exhibit strong X-ray variations by up to a factor of 100, coincident with their activity cycles (e.g. Favata et al. 2004), but, unlike $X_{\rm E}$, the X-ray luminosity of such stars is typically less than 10^{28} ergs s^{-1} and the observed activity time scale is several years. One possibility is that the strong variability of $X_{\rm E}$ could indicate abrupt activity produced by an enhanced mass accretion episode similar to that recently attributed to the outburst of the star in McNeil's nebula (Kastner et al. 2004). Indeed, the outburst increased the X-ray flux by a factor of 50, and the post-outburst X-ray luminosity of 10^{31} ergs s^{-1} is comparable to the luminosity of $X_{\rm E}$ during $\rm Obs_{XMM2}$.

The plasma temperature and X-ray luminosity of $X_{\rm E}$ exceed the typical quiescent X-ray activity of Class I protostars and are comparable to temperatures and luminosities of X-ray flares from Class I protostars (Imanishi et al. 2001; Shibata & Yokoyama 2002)[5]. X-ray flares from Class I protostars may be produced by reconnection in a magnetosphere which is twisted due to the core-disk differential rotation (Tsuboi et al. 2000; Montmerle et al. 2000). Perhaps a similar mechanism explains the X-ray emission from $X_{\rm E}$ during the *XMM-Newton* observations, though magnetic reconnection would have to occur throughout the *XMM-Newton* observations since no rapid X-ray variation was seen from $X_{\rm E}$.

The flux increase of a factor of two in ∼30 ksec in $\rm Obs_{XMM2}$ is unlike the types of variations seen in magnetically driven X-ray flares which are characterized by rapid (∼ 10 ksec) flux increases (e.g. Tsuboi et al. 1998, 2000; Stelzer et al. 2000; Imanishi et al. 2001). Favata et al. (2003) found a similar rise in X-ray brightness in the classical T-Tauri star XZ Tau, with a factor of 4 increase during 50 ksec. In this case, the brightening was accompanied by an $N_{\rm H}$ decrease and therefore Favata et al. (2003) interpreted it as an eclipse of the emitting region by the accretion stream. Because $X_{\rm E}$ did not show any significant hardness ratio variation the absorber would have to be uniformly dense, optically thick gas. Such a variation could be produced by an eclipse of the X-ray emitting region by an absorber

[5]Imanishi et al. (2001) used the distance to the ρ Oph cloud of 165 pc instead of 120 pc derived from more reliable *HIPPARCOS* data (Knude & Hϕg 1998) for a comparison to earlier X-ray results of the ρ Oph field. Their X-ray luminosity should be divided by a factor of two to compare to our result.

or emergence of the X-ray emitting region from behind the rim of the protostellar core as a result of stellar rotation.

If the fluorescent iron line in the spectra is real, this is unusual because fluorescent iron lines have been rarely observed from pre–main-sequence stars. Even a few examples during strong flares from Class I protostars have EW$\lesssim$ 150 eV (Imanishi et al. 2001). The large equivalent width of the fluorescent line from X_E ($\sim$250$-$800 eV) again suggests that the source is extremely embedded. When we simulate fluorescent iron line EWs, assuming solar abundance for the surrounding cold gas (Inoue 1985), an optically thick absorber should block the direct X-ray emission by $\sim$60% for Obs_{XMM1} and $\sim$3% for Obs_{XMM2}. This result is consistent with obscuration of the X-ray emission though the blocking factor in Obs_{XMM2} should be $\gtrsim$30% to explain the observed flux increase in Obs_{XMM2}. Interestingly, the intrinsic X-ray luminosity in Obs_{XMM1} should be log L_X $\sim$31.2 ergs s^{-1}, which is comparable to L_X in Obs_{XMM2}.

Our thermal model fit requires a metal abundance of $\sim$0.2 (0.1–0.3) solar. Though the derived abundance is dependent on the thermal model, and identifying emission lines in low resolution spectroscopy may be difficult especially around $\sim$1 keV (e.g. Kastner et al. 2002), the metal abundance of X_E is determined mostly from the iron K line region, which seems to show a real underabundance. X-ray emission from T Tauri stars similarly show sub-solar abundances (e.g., Favata et al. 2003). This might suggest that X_E has an X-ray emission mechanism similar to T Tauri stars. Such abundance anomalies could be produced by the FIP (first ionization potential) effect (e.g. Güdel et al. 2001). Unfortunately, the spectrum of X_E does not have enough counts to detect, unambiguously, emission lines from other elements such as argon and calcium to test the FIP effect. Another possible solution is that the continuum emission includes a non-thermal component, as proposed for ρ Oph S1 (Hamaguchi et al. 2003).

From the above discussion, we hypothesize that the X-ray plasma responsible for the hard component was produced at a mass accretion spot on the protostellar core. The X-ray emission is blocked when the spot would have been behind the protostellar core during Obs_{XMM1}, and just appeared from behind the rim in Obs_{XMM2} as a consequence of proto-stellar rotation (Figure 8). To be consistent with the observed *XMM-Newton* light curves, the rotational period of the proto-stellar core would need to be $\gtrsim$2.8 days. This rotation speed is much slower than the break-up rotation speculated for Class 0 protostars from rotational periods of Class I protostars (e.g. Montmerle et al. 2000).

The soft component was apparently constant and had much smaller N_H compared to the hard component. This may suggest that the component has no physical connection to, and exists far from, the hot component. One possible origin is that the soft component

is associated with another hidden protostar, but, though the $N_{\rm H}$ of the soft component is typical of Class I protostars, the K-band magnitude of $\gtrsim 19^m$ is much larger than those of Class I protostars in the R CrA cloud ($K \lesssim 11^m$). Another possible origin is that the X-ray plasma is heated by a collision of a steady jet or outflow from $\rm X_E$ with circumstellar gas, a mechanism thought to be associated with X-ray emission from HH2, L1551 IRS 5, and OMC 2/3 (Pravdo et al. 2001; Favata et al. 2003; Tsujimoto et al. 2004). Indeed, $\rm X_E$ is associated with a centimeter radio source as those systems are, but the plasma temperature and X-ray luminosity of $\rm X_E$ are very large compared to those sources, except for the source in OMC 2/3. Such a high plasma temperature requires an energetic jet with v_{jet} ∼1,500 km s^{-1}. While low-mass young stars generally have slow outflow velocities (a few hundred km s^{-1}), Marti et al. (1995) measured a large proper motion in the young stellar jets HH80-81 implying velocities up to 1,400 km s^{-1}. $\rm X_E$ could be another example of a source with high speed outflow.

6.2. What is $\rm X_W$?

$\rm X_W$ is a counterpart to the near-IR source IRS 7 as well as the centimeter radio source 10W. The column density of $\rm X_W$ ($\sim 2-6\times10^{23}$ cm^{-2}) is much larger than that typical of Class I protostars, while the K-band magnitude of $\sim 12.2^m$ is comparable to the brightness of Class I protostars in the R CrA cloud. Therefore, $\rm X_W$ might be a Class I source seen at a large inclination angle. On the other hand, IRS 7 had been suspected to be the counterpart of an X-ray flare source seen during an *ASCA* observation (Koyama et al. 1996). However, the $N_{\rm H}$ measured during the *ASCA* flare ($\sim 4\times10^{22}$ cm^{-2}) was significantly smaller than that of $\rm X_W$, even considering that the *ASCA* spectrum is contaminated by emission from surrounding Class I protostars with lower $N_{\rm H}$. If the *ASCA* flare source is really $\rm X_W$, the absorption column must be variable.

7. Summary & Conclusion

We discovered two extremely embedded X-ray sources at the positions of the strong VLA centimeter radio sources in the IRS 7 star forming core. Thanks to its vicinity to the Sun (d ∼170 pc), the large effective area of *XMM-Newton* and an opportunity to catch an active phase, we obtained around ∼2,000 photons from $\rm X_E$, which is about 40 times better than other extremely embedded X-ray sources observed so far. The upper-limit to the K-band luminosity was restricted to ∼1/150 of the extremely embedded protostars in the OMC-2/3 cloud (d ∼450 pc and completeness limit ∼16^m, Tsujimoto et al. 2003). This is therefore

a rare, high signal-to-noise X-ray detection of what appears to be a Class 0 protostar or a protostar in an intermediate phase between Class 0 and Class I. The combination of *XMM-Newton* and *Chandra* observations enabled us to study the X-ray emission mechanism in detail. The source showed a significant long-term X-ray variation by a factor of 10–100. The X-ray properties – kT ∼3−4 keV and log $L_{\rm X}$ ∼31 ergs s^{-1}– are comparable to magnetically active X-ray flaring sources though the light curve of $X_{\rm E}$ does not suggest flaring activity. These results may suggest that the X-ray activity was enhanced by mass accretion. The X-ray flux during $\rm Obs_{XMM2}$ increased monotonically by a factor of two in 30 ksec, and the X-ray spectra showed a strong iron fluorescent line with EW of 250–800 eV. These phenomena may be related to the partial blocking of the X-ray plasma or perhaps they are indicative of rotation of a hot spot on the proto-stellar core.

The evolutionary status of $X_{\rm E}$ should be constrained by constructing the IR and radio SED. This requires high spatial resolution and high sensitivity. Spitzer, ALMA, and 8 m class ground based telescopes are well-suited to examine this mysterious X-ray protostar. On the other hand, long exposure X-ray observations would confirm the fluorescent line profile and test the suggested periodicity in the X-ray brightness. These studies would help to understand the physical nature of protostars at the earliest phase.

We are grateful to M. Choi, T. Hunter, T. Yokoyama, K. Tatematsu, M. Tsujimoto, H. Murakami, K. Koyama, S. Yashiro, Y. Tsuboi, and the anonymous referee for useful comments. This work is performed while K.H. held awards by National Research Council Research Associateship Award at NASA/GSFC, and is supported by *XMM-Newton* US grant.

Facilities: XMM-Newton(EPIC), CXO(ACIS-I). UH88(QUIRC), SUBARU(IRCS+AO)

REFERENCES

Anderson, I. M., Harju, J., Knee, L. B. G., & Haikala, L. K. 1997, A&A, 321, 575

André, P., Ward-Thompson, D., & Barsony, M. 1993, ApJ, 406, 122

Aschenbach, B., Briel, U. G., Haberl, F., Bräuninger, H. W., Burkert, W., Oppitz, A., Gondoin, P., & Lumb, D. H. 2000, in SPIE, Vol. 4012, X-Ray Optics, Instruments, and Missions III, ed. Joachim E. Trümper, Bernd Aschenbach, p. 731–739

Brown, A. 1987, ApJ, 322, L31

Chini, R., et al. 2003, A&A, 409, 235

Choi, M., & Tatematsu, K. 2004, ApJ, 600, L55

Favata, F., Giardino, G., Micela, G., Sciortino, S., & Damiani, F. 2003, A&A, 403, 187

Favata, F., Micela, G., Baliunas, S. L., Schmitt, J. H. M. M., Güdel, M., Harnden, , F. R., Sciortino, S., & Stern, R. A. 2004, A&A, 418, L13

Feigelson, E. D., Carkner, L., & Wilking, B. A. 1998, ApJ, 494, L215

Garmire, G., & Garmire, A. 2002, APS Meeting Abstracts, 17064

Grosso, N., Montmerle, T., Feigelson, E. D., André, P., Casanova, S., & Gregorio-Hetem, J. 1997, Nature, 387, 56

Güdel, M., et al. 2001, in Proceedings of the 12th Cambridge Workshop of Cool Stars, Stellar Systems, and the Sun: The Future of Cool-Star Astrophysics, ed. A. Brown, T. R. Ayres, & G. M. Harper, Boulder: Univ. of Colorado, in press

Hamaguchi, K., Corcoran, M. F., & Imanishi, K. 2003, PASJ, 55, 981

Harju, J., Haikala, L. K., Mattila, K., Mauersberger, R., Booth, R. S., & Nordh, H. L. 1993, A&A, 278, 569

Harju, J., Higdon, J. L., Lehtinen, K., & Juvela, M. 2001, in ASP Conf. Ser. 235: Science with the Atacama Large Millimeter Array, ed. A. Wootten, p. 125–129

Henning, T., Launhardt, R., Steinacker, J., & Thamm, E. 1994, A&A, 291, 546

Imanishi, K., Koyama, K., & Tsuboi, Y. 2001, ApJ, 557, 747

Inoue, H. 1985, Space Science Reviews, 40, 317

Jansen, F., et al. 2001, A&A, 365, L1

Kastner, J. H., Huenemoerder, D. P., Schulz, N. S., Canizares, C. R., & Weintraub, D. A. 2002, ApJ, 567, 434

Kastner, J. H., et al. 2004, Nature, 430, 429

Knude, J., & Hϕg, E. 1998, A&A, 338, 897

Koyama, K., Hamaguchi, K., Ueno, S., Kobayashi, N., & Feigelson, E. D. 1996, PASJ, 48, L87

Marti, J., Rodriguez, L. F., & Reipurth, B. 1995, ApJ, 449, 184

McClintock, J. E., & Remillard, R. A. 2003, astro-ph/0306213

Mewe, R., Kaastra, J. S., & Liedahl, D. A. 1995, Legacy, 6, 16

Montmerle, T., Grosso, N., Tsuboi, Y., & Koyama, K. 2000, ApJ, 532, 1097

Morrison, R., & McCammon, D. 1983, ApJ, 270, 119

Pravdo, S. H., Feigelson, E. D., Garmire, G., Maeda, Y., Tsuboi, Y., & Bally, J. 2001, Nature, 413, 708

Rho, J., Ramírez, S. V., Corcoran, M. F., Hamaguchi, K., & Lefloch, B. 2004, ApJ, 607, 904

Saraceno, P., André, P., Ceccarelli, C., Griffin, M., & Molinari, S. 1996, A&A, 309, 827

Shibata, K., & Yokoyama, T. 2002, ApJ, 577, 422

Skinner, S., Gagné, M., & Belzer, E. 2003, ApJ, 598, 375

Stelzer, B., Neuhäuser, R., & Hambaryan, V. 2000, A&A, 356, 949

Stern, R. A. 1998, in ASP Conf. Ser. 154: Cool Stars, Stellar Systems, and the Sun, 223–+

Strüder, L., et al. 2001, A&A, 365, L18

Townsley, L. K., Broos, P. S., Garmire, G. P., & Nousek, J. A. 2000, ApJ, 534, L139

Tsuboi, Y., Imanishi, K., Koyama, K., Grosso, N., & Montmerle, T. 2000, ApJ, 532, 1089

Tsuboi, Y., Koyama, K., Hamaguchi, K., Tatematsu, K., Sekimoto, Y., Bally, J., & Reipurth, B. 2001, ApJ, 554, 734

Tsuboi, Y., Koyama, K., Murakami, H., Hayashi, M., Skinner, S., & Ueno, S. 1998, ApJ, 503, 894

Tsujimoto, M., Koyama, K., Kobayashi, N., Goto, M., Tsuboi, Y., & Tokunaga, A. T. 2003, AJ, 125, 1537

Tsujimoto, M., Koyama, K., Kobayashi, N., Saito, M., Tsuboi, Y., & Chandler, C. J. 2004, PASJ, 56, 341

Turner, M. J. L., et al. 2001, A&A, 365, L27

Ueda, Y., et al. 1998, Nature, 391, 866

van den Ancker, M. E. 1999, PhD thesis, Universiteit van Amsterdam

Weisskopf, M. C., Brinkman, B., Canizares, C., Garmire, G., Murray, S., & Van Speybroeck, L. P. 2002, PASP, 114, 1

Wilking, B. A., McCaughrean, M. J., Burton, M. G., Giblin, T., Rayner, J. T., & Zinnecker, H. 1997, AJ, 114, 2029, (W97)

This preprint was prepared with the AAS LaTeX macros v5.2.

Table 1. Observation Logs

Observation	Observatory	Seq. ID	Date	Exposure (ksec)	Δ_{axis}	Shift ($\Delta\alpha$,$\Delta\delta$)
Obs_{XMM1}	*XMM-Newton*	146390101	2003 Mar. 28	14.9/21.5	$6'$	($0.''$ 4, $-1.''$ 0)
Obs_{XMM2}	*XMM-Newton*	146390201	2003 Mar. 29	18.1/24.0	$6'$	($0.''$ 2, $-1.''$ 3)
Obs_{CXO1}	*Chandra*	200017	2000 Oct. 7	19.7	$2'$	($0.''$ 03, $0.''$ 23)
Obs_{CXO2}	*Chandra*	200194	2003 Jun. 26	37.6	$0.'$ 2	($0.''$ 42, $-0.''$ 03)

Note. — Exposure: EPIC pn/MOS for *XMM-Newton*. Δ_{axis}: Off-axis angle of the IRS7 region. Objects used for the position correction: IRS2, IRS5, HBC677, CrA1, ISO-CrA136, HH101 IRS 4, ISO-CrA137, TY CrA and HD 176386. IRS1 and ISO-CrA134 were also used for the position correction of the *Chandra* data.

Table 2. Detected Sources

Source	Designation	Observation	(α_{2000}, δ_{2000})[a] (h m s, d $'$ $''$)	Net cnts (cnts)	K-band (mag)	Counterpart
X_E	XMMU J190156.3-365726	Obs_{XMM1}	19 1 56.29, −36 57 26.5	467.7	$\gtrsim$19.4	10E[d] , vdA 5(?)[e]
		Obs_{XMM2}	19 1 56.32, −36 57 26.4	1611.3	···	···
	CXOU J190156.4-365728	Obs_{CXO1}	19 1 56.43, −36 57 27.7	19.6	···	···
		Obs_{CXO2}	19 1 56.39, −36 57 28.3	12.7	···	···
X_W	XMMU J190155.3-365721	$Obs_{XMM1\&2}$	19 1 55.26, −36 57 20.8	114.0[b]	12.2[c]	10W[d] , Source 4[f] , IRS7, vdA 3(?)[e]
	CXOU J190155.3-365722	Obs_{CXO1}	19 1 55.34, −36 57 21.6	12.7	···	···
		Obs_{CXO2}	19 1 55.32, −36 57 21.8	22.4	···	···

Note. — Net cnts: EPIC pn + MOS for *XMM-Newton*.

[a]Positional uncertaintiess are $\sim 2''$ for *XMM-Newton* and $\sim 1''$ for *Chandra*.

[b]Net counts in Obs_{XMM1}.

[c]Reference of the K$'$ magnitude of R1 (IRS 7) to Wilking et al. (1997).

[d]Reference to Brown (1987) and Feigelson et al. (1998).

[e]Reference to van den Ancker (1999).

[f]Reference to Choi & Tatematsu (2004).

Table 3. Fitting Result of the X_E Light Curve

Observation	Binning (sec)	Model	Constant (10^{-2} cnts s^{-1})	Linear (10^{-2} cnts s^{-1} day^{-1})	χ^2/d.o.f. (d.o.f.)
Obs_{XMM1}	2,000	constant	0.93	···	1.63 (13)
Obs_{XMM2}	1,000	constant	5.3	···	1.96 (26)
	1,000	constant+linear	3.7[a]	9.3	1.21 (25)

[a]Count rate at TJD = 12727.8564 day.

Table 4. Fitting Results of the Spectra

Source	Observation	Model	Comp.	$N_{\rm H}$ ($10^{22}{\rm cm}^{-2}$)	kT (keV)	Abundance (solar)	log $E.M.$ (${\rm cm}^{-3}$)	Flux$_{6.4keV}$ (10^{-6} cnts ${\rm cm}^{-2}$ ${\rm s}^{-1}$)	χ^2/d.o.f. (d.o.f)	log $L_{\rm X}$ (ergs ${\rm s}^{-1}$)
$X_{\rm E}$	Obs_{XMM1}	A(1T)		13.2 (9.6−18.3)	5.1 (2.8−10.4)	0.5 (0.2−1.4)	53.2 (53.0−53.6)	2.4	1.22 (21)	30.4
	Obs_{XMM2}	B(1T)		24.7 (21.6−28.3)	4.4 (3.4−6.1)	0.2 (0.1−0.3)	54.1 (54.0−54.1)	3.4	0.99 (66)	31.2
	$Obs_{XMM1\&2}$	C(2T)	Var_1	28.1 (22.5−33.8)	2.7 (1.8−4.2)	0.2 (0.1−0.3)	53.8 (53.5−54.1)	2.8 (0.8−4.8)	0.97 (86)	30.8
			Var_2	$=Var_1$	4.0 (2.9−5.3)	$=Var_1$	54.1 (54.0−54.4)	3.4 (1.4−5.5)	···	31.2
			Const.	4.2 (1.4−11.4)	2.3 (0.4−)	$=Var_1$	52.5 (51.8−53.5)	···	···	29.6
$X_{\rm W}$	Obs_{XMM1}	D(1T)		33.7 (19.1−60.0)	4.7 (1.6−)	0.3 (fix)	53.3 (52.8−54.3)	···	0.65 (8)	30.5
	$Obs_{CXO1\&2}$	E(1T)		33.7 (fix)	4.7 (fix)	0.3 (fix)	52.9 (52.8−53.0)	···	0.60 (3)	30.0

Note. — $Var_{1(2)}$: variable hard component in Obs_{XMM1} (Obs_{XMM2}). Const.: constant soft component. $L_{\rm X}$: absorption corrected X-ray luminosity in the 0.5−10 keV band. Distance assumes d ∼170 pc.

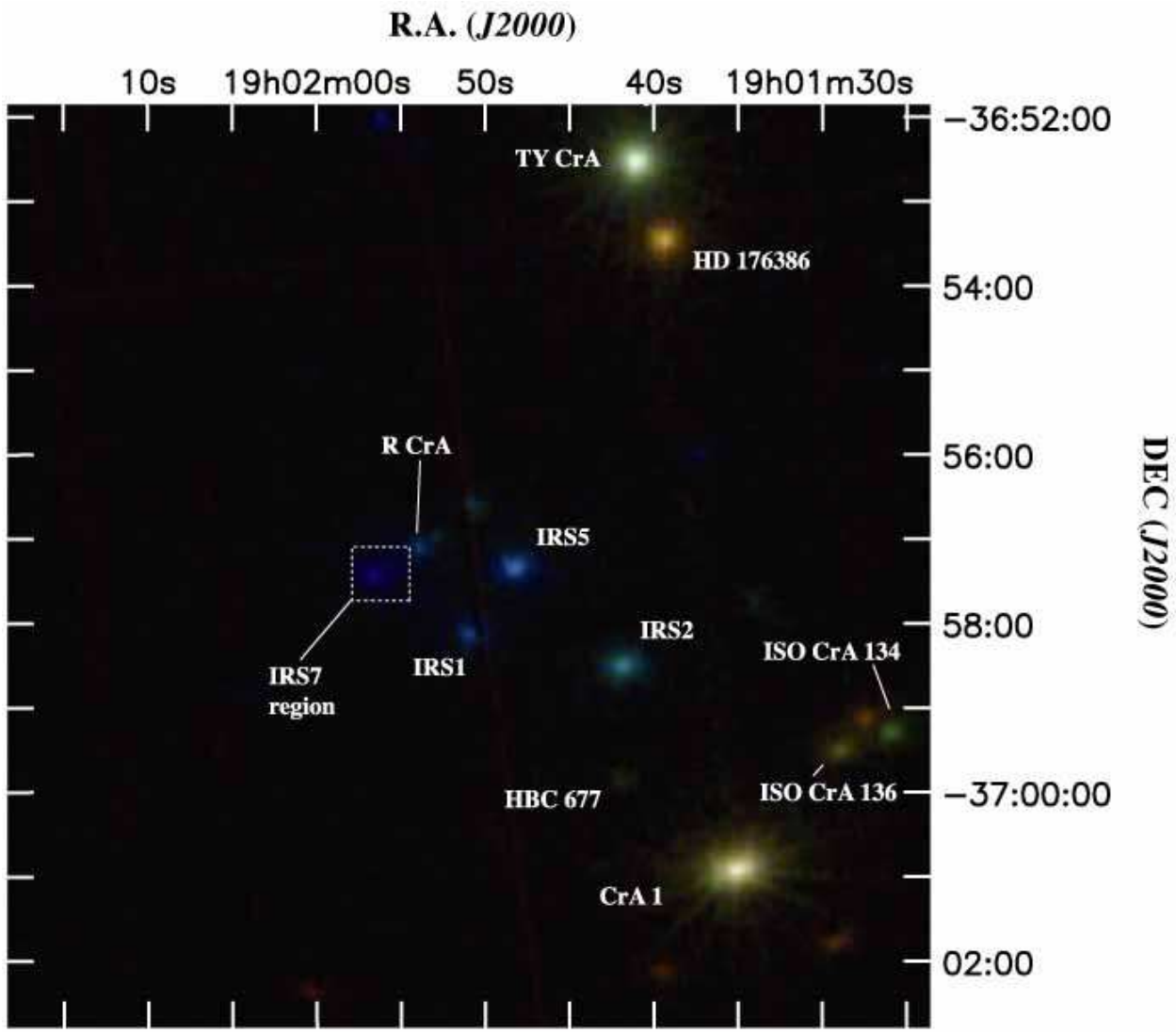

Fig. 1.— *XMM-Newton* "true-color" image of the R CrA star forming region ($\mathrm{Obs_{XMM1}}$ + $\mathrm{Obs_{XMM2}}$). The image is color coded to represent hard band (3−9 keV) to blue, medium band (1−3 keV) to green, and soft band (0.2−1 keV) to red. The dotted rectangle shows the IRS 7 region (field of view of Figure 2 except the bottom right panel). Class I protostar: IRS 1, IRS 2, IRS 5, Herbig Ae/Be star: R CrA, TY CrA, HD 176386, Weak-lined T-Tauri star: CrA 1.

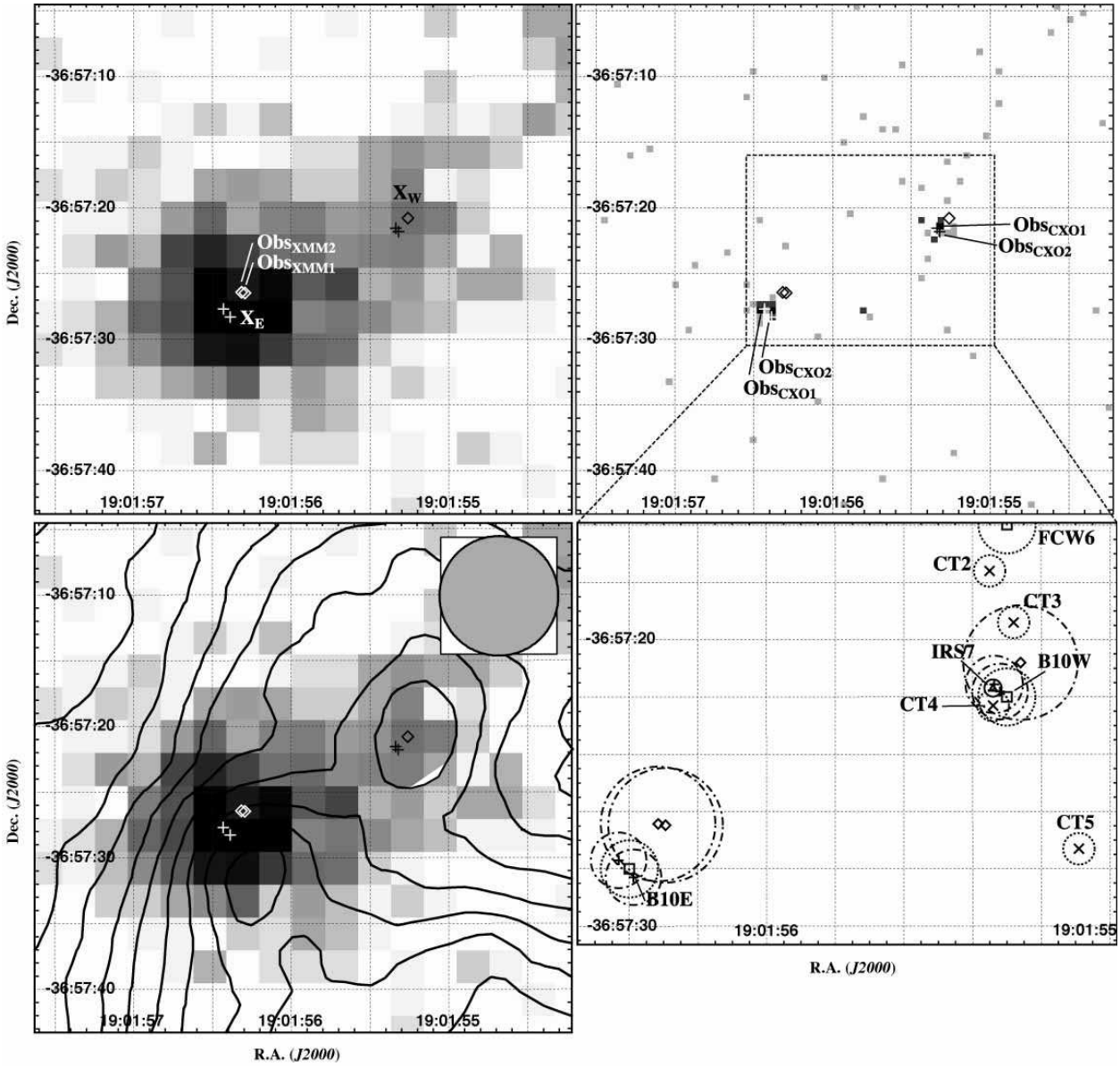

Fig. 2.— Magnified images of the IRS 7 region. The top left panel: the 3−9 keV EPIC pn + MOS image of *XMM-Newton* combining $\mathrm{Obs_{XMM1}}$ and $\mathrm{Obs_{XMM2}}$, the top right panel: the 0.5−9 keV image of *Chandra* in $\mathrm{Obs_{CXO1}}$, the bottom left panel: the *XMM-Newton* image overlaying flux contours in sub-millimeter at 450 μm taken by van den Ancker (1999), the bottom right panel: source positions with their error circles including sources in near-IR and radio wavelengths. Diamonds show *XMM-Newton* sources, crosses *Chandra* sources, squares centimeter radio sources (B*number*: Brown 1987, FCW*number*: Feigelson et al. 1998, Source positions are referred to Feigelson et al. 1998), x millimeter radio sources (CT*number*: Choi & Tatematsu 2004), a triangle near-IR source (IRS 7). The gray circle in the bottom left panel shows the beam size of the sub-millimeter telescope. Error circles in the bottom right panel are drown in dot-bar line for X-ray sources, dotted line for radio sources, and solid line for the near-IR source IRS 7.

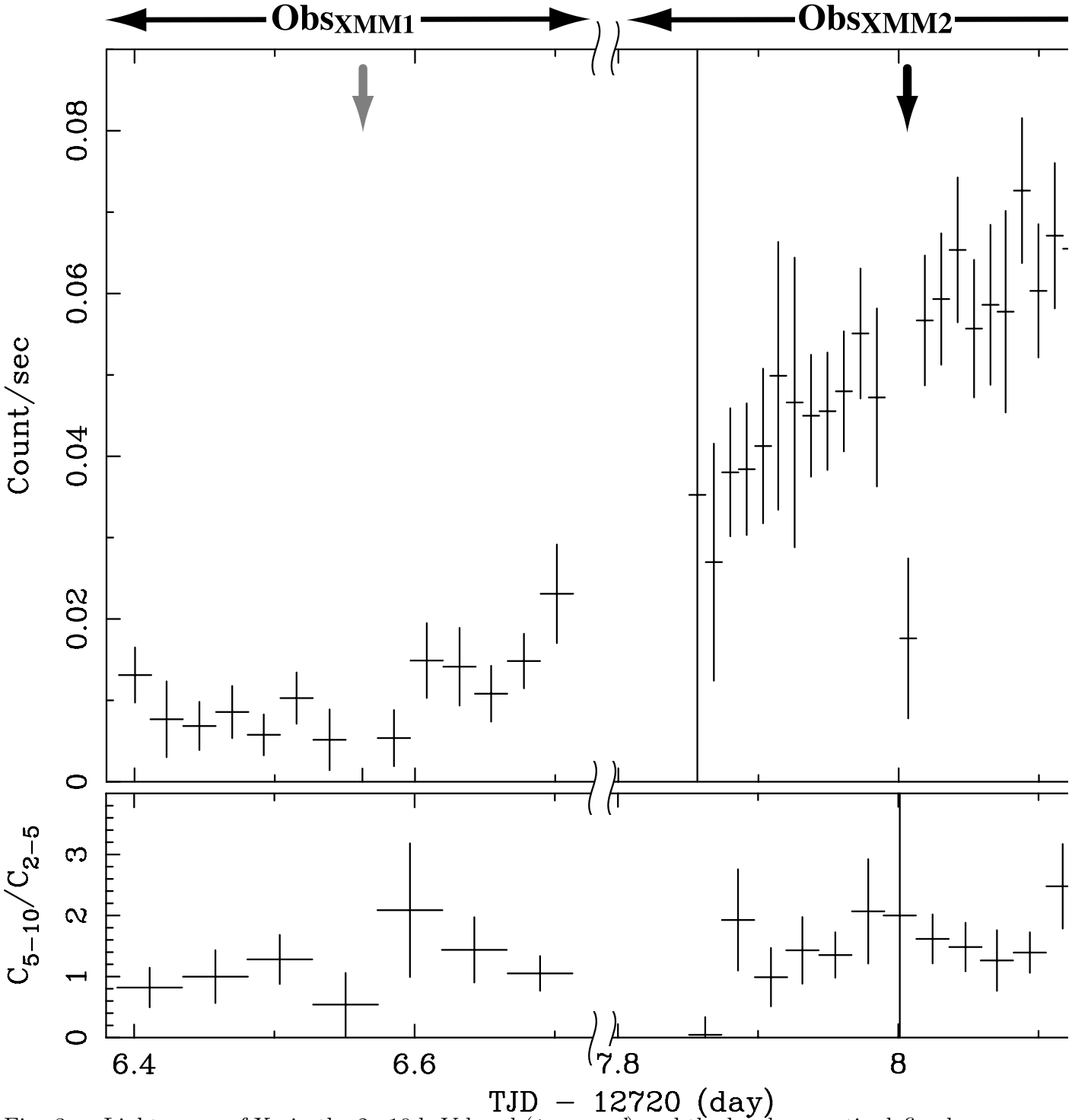

Fig. 3.— Light curve of X_E in the 2−10 keV band (*top panel*) and the hardness ratio defined as "count rates in the 5−10 keV band / count rates in the 2−5 keV band" (*bottom panel*). Points with error bars in the top and bottom panels are made from summed data sets of EPIC pn plus MOS (1+2). The horizontal axis is truncated Julian day (TJD) − 12720. The arrows show timings of the dip feature. Bins in the top panel have 2 ksec for Obs_{XMM1} and 1 ksec for Obs_{XMM2}, and bins in the bottom panel have 4 ksec for Obs_{XMM1} and 2 ksec for Obs_{XMM2}.

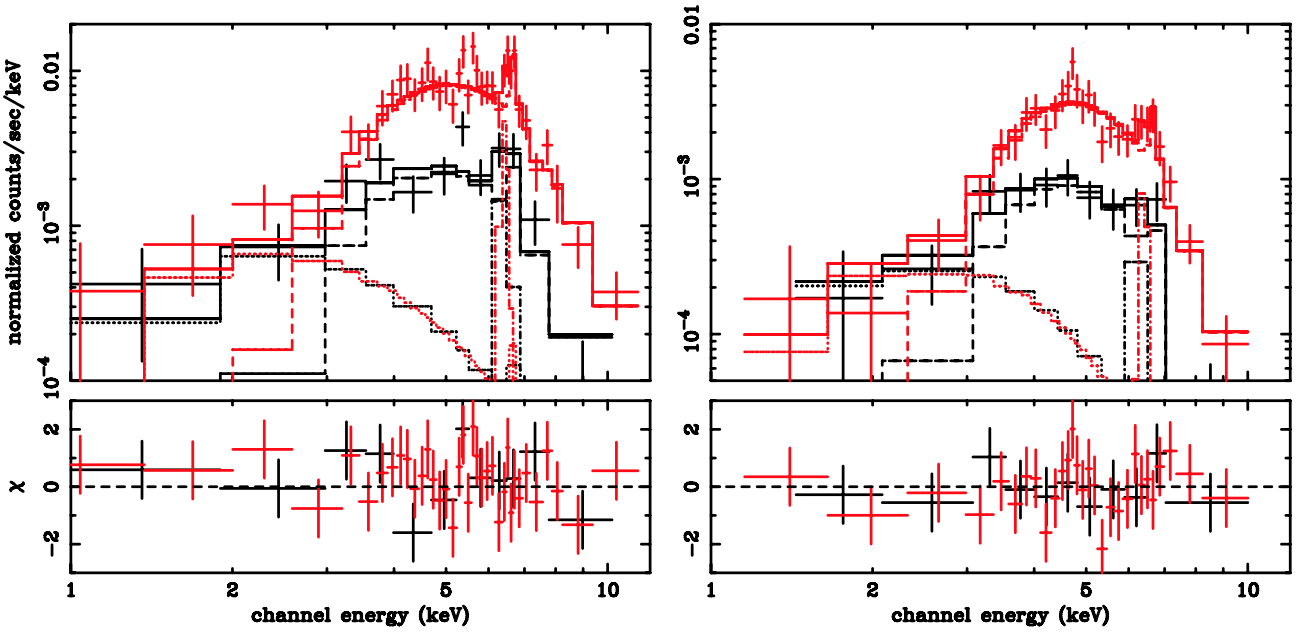

Fig. 4.— EPIC pn (*left*) and MOS (1+2) (*right*) spectra of X_E in Obs_{XMM1} (*black*) and Obs_{XMM2} (*red*). The solid lines show the best-fit model of the simultaneous fitting with EPIC pn and MOS. Dotted lines show the soft component, barred line the hard component, and dot-bar lines the Gaussian component for the line at 6.4 keV. Each bottom panel shows the residuals of the χ^2 fit.

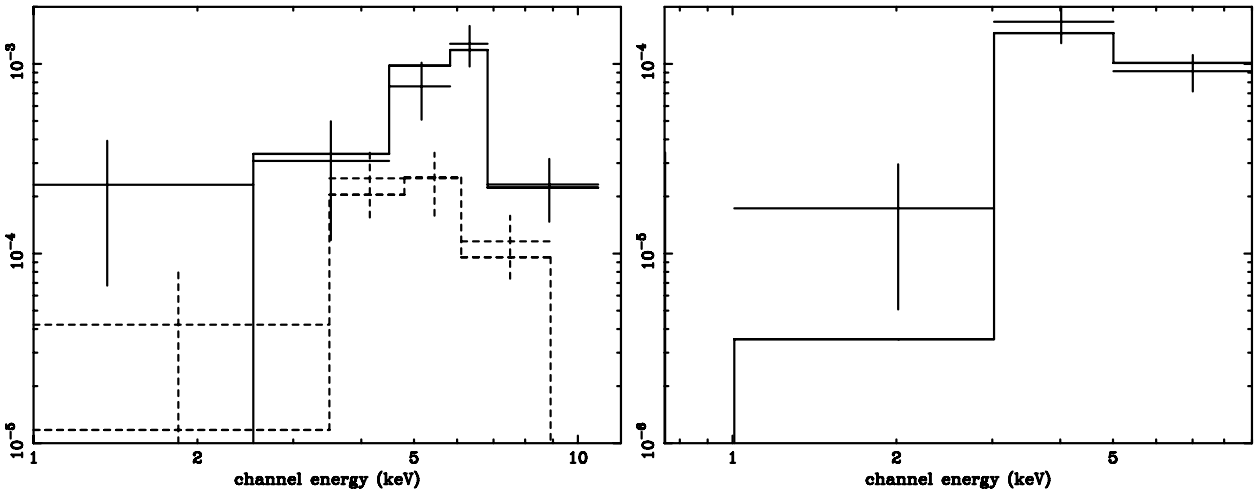

Fig. 5.— X_W spectra in Obs_{XMM1} (*left*, solid – pn, dot – MOS) and Obs_{CXO1} plus Obs_{CXO2} (*right*). Both panels show data points and their best-fit models (Model D and E in Table 4 from left).

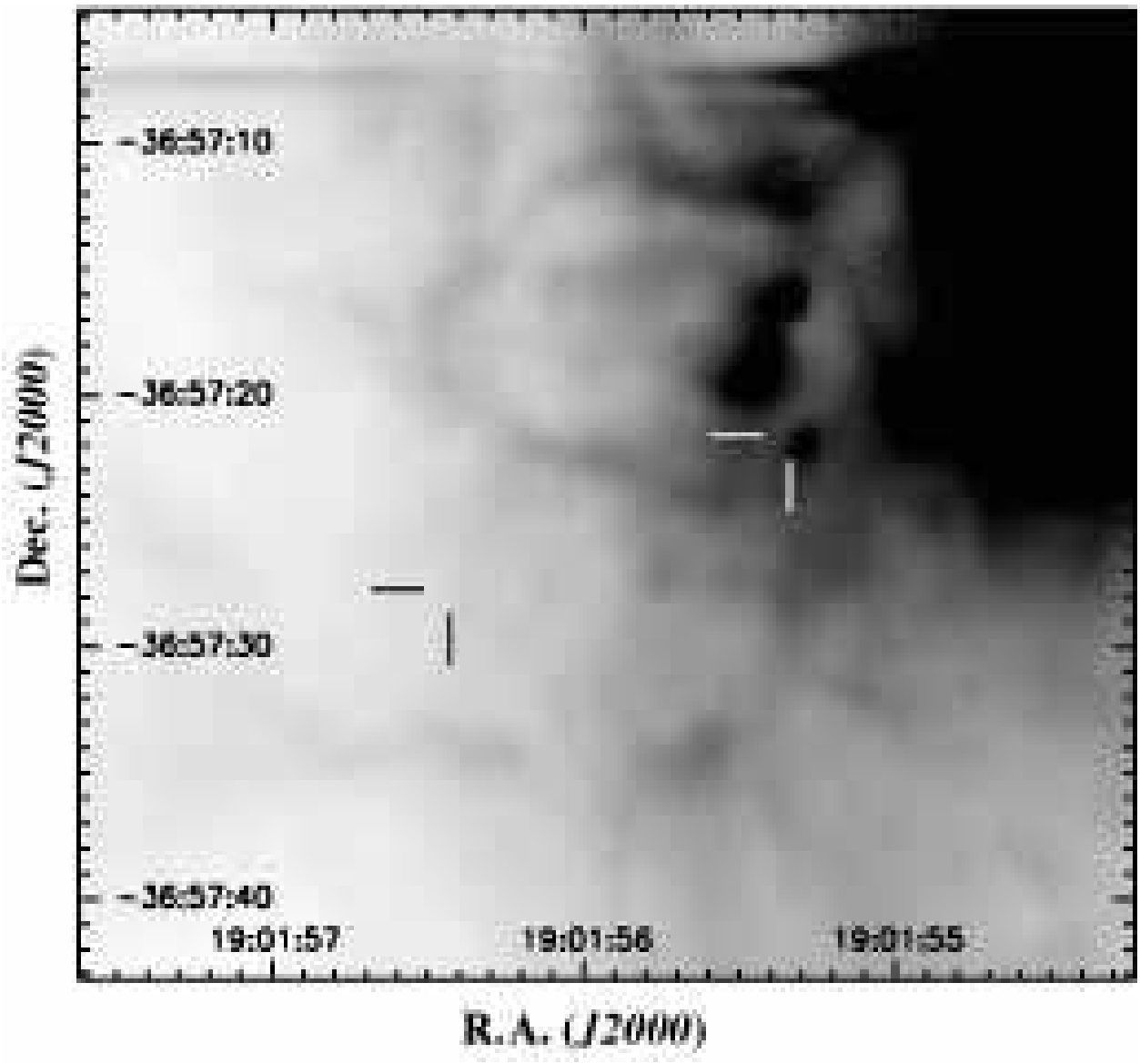

Fig. 6.— K-band image of the IRS 7 region obtained in 1998. The X_E and X_W positions measure with *Chandra* are at the left and right crosses, respectively.

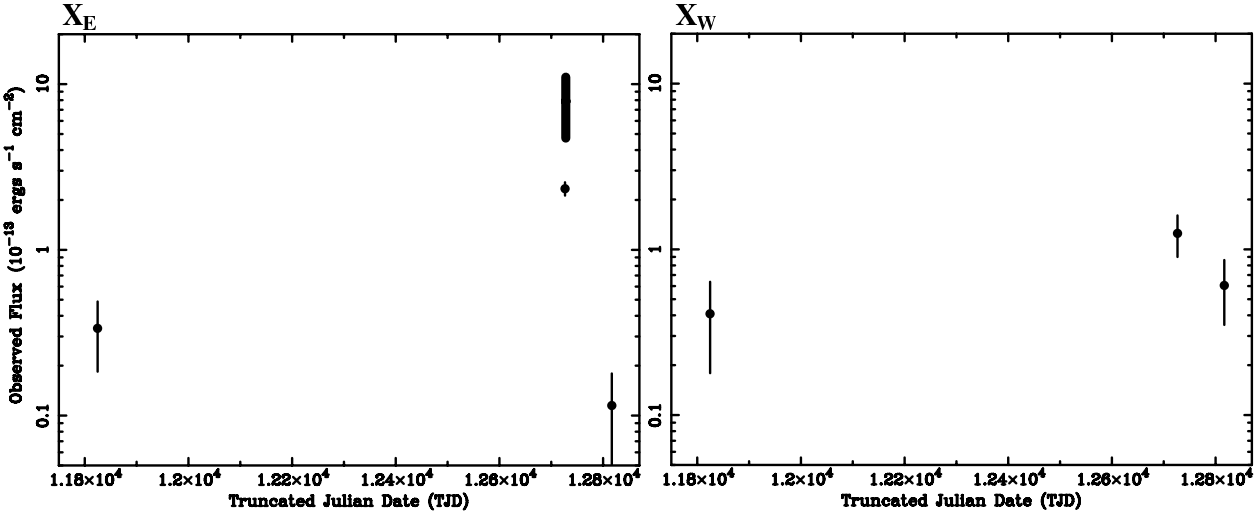

Fig. 7.— Observed X-ray flux between 0.5–10 keV in long time scale (*left*: X_E, *right*: X_W). The vertical narrow bars on the data points show photon statistical error at 90% confidence level. The thick bar shows the variable range of X_E during Obs_{XMM2}.

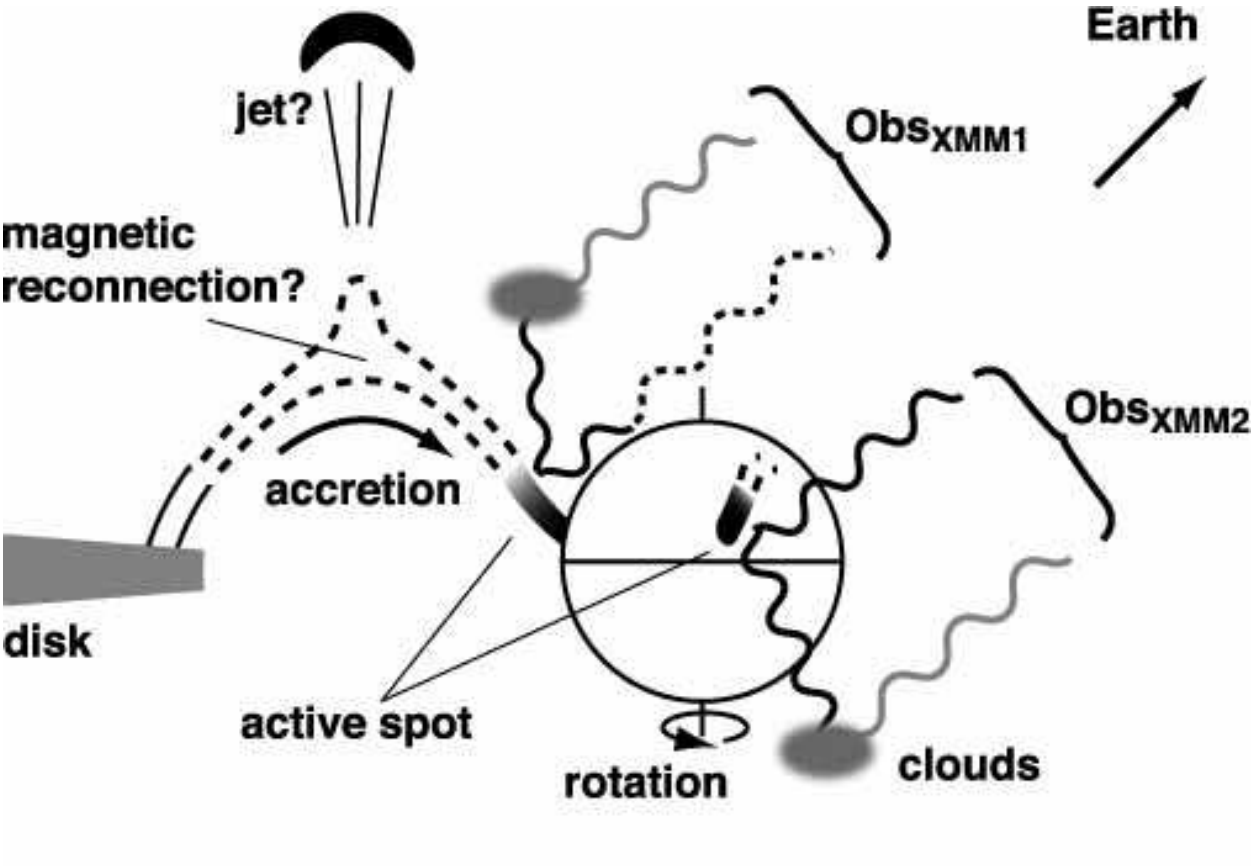

Fig. 8.— Possible geometry of the proto-stellar core, jet, and observer . The wavy lines show X-ray emission (solid black: direct X-rays, grey: fluorescent and scattering X-rays, dotted black: direct X-rays are partially covered).